RESEARCH PAPER

Silicon nanoparticles produced by spark discharge

Vincent A. Vons · Louis C. P. M. de Smet ·
David Munao · Alper Evirgen · Erik M. Kelder ·
Andreas Schmidt-Ott

Abstract On the example of silicon, the production of nanoparticles using spark discharge is shown to be feasible for semiconductors. The discharge circuit is modelled as a damped oscillator circuit. This analysis reveals that the electrode resistance should be kept low enough to limit energy loss by Joule heating and to enable effective nanoparticle production. The use of doped electrodes results in a thousand-fold increase in the mass production rate as compared to intrinsic silicon. Pure and oxidised uniformly sized silicon nanoparticles with a primary particle diameter of 3–5 nm are produced. It is shown that the colour of the particles can be used as a good indicator of the oxidation state. If oxygen and water are banned from the spark generation system by (a) gas purification, (b) outgassing and (c) by initially using the particles produced as getters, unoxidised Si particles are obtained. They exhibit pyrophoric behaviour. This continuous nanoparticle preparation method can be combined with other processing techniques, including

surface functionalization or the immediate impaction of freshly prepared nanoparticles onto a substrate for applications in the field of batteries, hydrogen storage or sensors.

Introduction

Over the last decades research on nanoparticles has increased tremendously (Goesmann and Feldmann 2010). Nanoparticles are currently being studied and exploited in a wide variety of applications, including catalysis, (Burda et al. 2005) solar cells and photovoltaics (Günes et al. 2007), biology and medicine (De et al. 2008), energy conversion and storage (Arico et al. 2005), and sensor devices (Asefa et al. 2009). In these applications, nanoparticles are applied as a suspension or a powder or they are used as building blocks to construct nanostructured (hybrid) architectures, e.g. via self-assembling processes or thin film deposition techniques. Various metal and semiconductor materials have been used as nanoparticle core materials. For example, II–VI (ZnSe, CdTe or SnTe) and II–V materials (InP and GaAs) can be used to prepare so-called core–shell semiconductor nanoparticles, often referred to as quantum dots. Alternatively, semiconductor nanoparticles can be

V. A. Vons · D. Munao · A. Evirgen ·
E. M. Kelder · A. Schmidt-Ott (✉)
Department of Chemical Engineering, Nano-Structured Materials, Delft University of Technology,
Julianalaan 136, 2628 BL Delft, The Netherlands
e-mail: a.schmidt-ott@tudelft.nl

L. C. P. M. de Smet · A. Evirgen
Department of Chemical Engineering, Nano-Organic Chemistry, Delft University of Technology,
Julianalaan 136, 2628 BL Delft, The Netherlands

prepared from silicon (Si), which is not only more abundant, but also cheaper and less toxic as compared to any other semiconductor material. Moreover, SiO_2 and hydrogen-terminated Si allow covalent (bio)functionalization using silane and hydrosilylation chemistry, respectively (Aswal et al. 2006; Buriak 2002) making silicon nanoparticles (SiNPs) attractive for various applications.

Silicon nanoparticles are particularly interesting in view of the developments in the field of energy storage and sensing devices. For example, in Li-ion batteries, Si is interesting as an anode material, because it can accommodate 4.4 Li atoms per Si atom, resulting in a theoretical capacity of 4200 $mAhg^{-1}$ instead of the ~ 370 $mAhg^{-1}$ of currently used graphite anodes. However, the resultant volume expansion of up to 300% has prevented the application of silicon in battery materials (Ding et al. 2009). Due to their very high surface-to-volume ratio, nanoparticles offer more contact with the current collector in battery assembly as compared to bulk materials. The small absolute volume expansion of NPs will decrease the breakup of the battery structure and thus increase battery life (Kasavajjula et al. 2007). In addition, for hydrogen storage on board vehicles, Si is interesting, since it can destabilise magnesium hydride (MgH_2) (Janot et al. 2006). This results in a much lower heat requirement and a 1 bar pressure plateau at ~ 20 °C. However, this system still suffers from poor reversibility. A reduction of the particle size will result in higher reactivity and much shorter diffusion distances, and will thus very likely increase reversibility very significantly. In the field of sensing, Si and SiO_2 NPs can be exploited (Ghoshal et al. 2010) as fluorescent markers/bioprobes (Burns et al. 2006) or as building blocks for construction of nanostructured silicon layers, for example, to make a UV photodetector (Nayfeh et al. 2004). Porous silicon (Canham 1990) has been applied in optical (Ben-Chorin et al. 1994; Létant and Sailor 2000) and electrical (Ben-Chorin et al. 1994; Foucaran et al. 1997; Watanabe et al. 1996) sensor platforms.

Nanoparticles can be produced via different methods (O'Farrell et al. 2006; Masala and Seshadri 2004) including vapour-based physical approaches and solution-based chemical approaches. Alternatively, top-down reduction methods are used. In the case of silicon, bottom-up approaches include the use of supercritical fluids, laser-driven pyrolysis, solution phase oxidation–reduction methods, the synthesis in

reversed micelles and laser ablation. Examples of bulk reduction methods are ultrasonication of porous silicon substrates, electrochemical deposition and the annealing of SiO powders.

As a vapour-based approach, spark discharge generation (SDG) was introduced by Schwyn et al. (Schwyn et al. 1988) as a method for nanoparticle production. Here a high voltage gas break-down is repeatedly induced between two electrodes of the desired material. Usually, the energy stored in a capacitor is released into the discharge very rapidly, resulting in very high temperatures (typically 20,000 K). Interaction of the high temperature plasma with the electrode surfaces results in evaporation of the electrode material. As the discharge dies out, the vapour cloud cools very rapidly, first through adiabatic expansion and radiation and then by thermal conduction. The extremely high cooling rates result in a high concentration of very small particles of rather narrow size distribution (Tabrizi et al. 2009a). The nanoparticles formed are transported away by a flow of carrier gas. Basically, the only requirement for the starting material is that it should have a sufficient conductivity to carry the current to the spark gap. By choice of the electrodes various nanostructured materials can be obtained, both pure and mixed (Byeon et al. 2008; Tabrizi et al. 2010; Tabrizi et al. 2009a, b). Oxides can be obtained by adding oxygen to the carrier gas (Simonin et al. 2007).

The absence of liquid solvents together with the high thermal stability of gases involved in this process makes SDG an attractive alternative to produce highly pure silicon particles. Precursors, which are expensive and often hazardous, such as SiH_4 are avoided. The primary particle size of SDG-prepared particles is typically 1–10 nm (Byeon et al. 2008; Schwyn et al. 1988; Tabrizi et al. 2009a). Regarding this size range, application of SDG-prepared SiNPs would greatly increase the reaction rates in battery and hydrogen storage applications and the sensitivity of sensors. Finally, as the particles are generated in a continuous process in the form of an aerosol, SDG can be matched very well with other techniques for further processing of the nanoparticles. For example, the surface of the particles can be functionalised with many different components in the gas phase using a furnace reactor as suggested by Liao and Roberts (Liao and Roberts 2006). In addition, subsequent formation of highly porous but

rigid layers is possible using inertial impaction (Peineke and Schmidt-Ott 2006). Very recently, highly sensitive hydrogen gas sensors have been produced in our laboratory from spark generated palladium nanoparticles using inertial impaction (Biskos et al. 2010).

To our knowledge, so-far no work has been published on spark-generated semiconductor material. In this article, we report on a systematic investigation of producing silicon nanoparticles by spark discharge including electrical characterisation of the circuit, plasma appearance and particle size distributions for different types of silicon electrodes and electrode configurations. In addition, we characterised the SiNPs by TEM and XRD and report on the necessary measures to produce pure SiNPs.

Experimental

A spark discharge generator (Fig. 1) was used in combination with different silicon electrodes. Intrinsic silicon rods (99.95% wt. purity, 8 mm in diameter and 6 cm in length) were purchased from Alfa Aesar and p-type Si rods (6 mm in diameter and 6 cm in length, with a resistivity of 0.17 Ω cm) were obtained from SiMat Company. For comparison with a typical metal, a set of magnesium rods were used as well (99.9+% pure, 6.35 mm diameter and 8 cm length, Mateck GmbH). A Technix CCR-5-P-150, 0–5 kV, positive output, maximum 60 mA DC high voltage power supply is applied as a constant current source. It charges a capacitor consisting of a combination of commercial high voltage capacitors in a capacitor bank. A constant value of 20 nF was used for the present experiments. The electrodes are mounted inside a standard CF-35 vacuum flange 5-way cross.
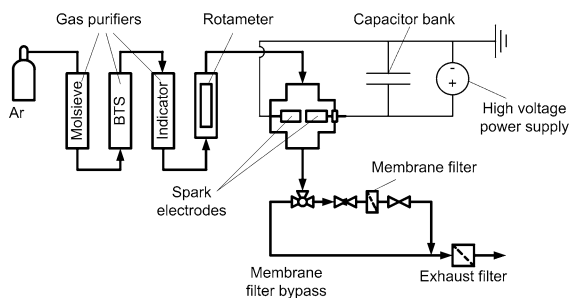

Fig. 1 Setup for production and collection of silicon nanoparticles. See experimental section for details

A micrometric screw on the ground electrode allows setting of the desired gap spacing, which was typically 2 mm here. The other arms of the cross hold the high voltage electrode, a glass viewport to observe the spark and lines for the carrier gas.

Analysis of the production rate

Argon 5.0 was used as a carrier gas at flow rates between 1 and 1.6 standard litres/min. The voltage across the capacitor (V_C) and the current through the plasma of the spark generator (I_{SG}) were measured using a Tektronix P6015 high-frequency, high-voltage probe (3.0 pF capacitance) and a Pearson 110 current probe connected to a LeCroy 9354 500 MHz oscilloscope. This oscilloscope was connected to a computer in order to record the observed waveforms. The spark generator was run between 100 and 300 Hz (sparks per second). To obtain a measure of the particle production rate, a TSI 3071 Differential Mobility Analyzer (DMA) equipped with a Kr-85 neutralizer, was used in combination with a condensation particle counter (CPC) or a Faraday cup aerosol electrometer (AEM) to determine particle size distributions (PSDs). The neutralizer establishes a known charge distribution on the particles. To calculate the fraction of positive, negative, and neutral particles and so obtain the total size distribution, the ion mobility and mass as given by Wiedensohler and Fissan for Ar gas were used (Wiedensohler and Fissan 1988, 1991).

Production and analysis of silicon nanoparticles

Extensive measures were taken to prevent contact of the particles with oxygen and water. To prevent oxygen and/or water from diffusing through the walls or through rubber O-rings the entire setup was constructed from stainless steel components, using metal-on-metal seals and leak-tested using a helium leak detector. The argon 5.0 carrier gas is first passed through a molecular sieve bed (4 Å) to remove any traces of water, behind which a copper-based catalyst (BASF R3-11 BTS catalyst) removes oxygen. Finally, the gas passes through a commercial absorber (Alltech indicating oxygen trap), for which an outlet concentration for oxygen of <1 ppb is specified. Prior to any experiments the setup was baked out at 100 °C under flowing Ar gas to remove

water adsorbed to the walls. To remove any remaining traces of oxygen and water, silicon production was started ∼1 h before particle collection, bypassing the collection filter. This way, the gettering action of the particles was used to remove any oxidizing species in the system. This also helps to remove any oxide layer covering the electrodes. The system is kept at a pressure slightly above atmospheric, ensuring that gas flows out of the system rather than inwards through any remaining tiny leaks. Particles are collected from the gas phase on membrane filters (Millipore Durapore 0.45 μm PVDF filters) mounted perpendicular to the gas flow ∼20 cm downstream of the spark generator in a special filter holder. A flow diagram of the test set-up is given in Fig. 1.

After collection the filter holder was closed off using plug valves, disconnected from the setup and transferred to an argon-filled glovebox with O_2 and H_2O concentrations of <0.1 ppm. The collected particles were analysed using Transmission Electron Microscopy (TEM) on a FEI Monochromated Tecnai 200 STEM-FEG, to determine the primary particle size and particle morphology. Powder X-ray diffraction (XRD) spectra were taken using CuKα radiation on a Bruker D8-Advance X-Ray Diffractometer operated at 40 kV and 40 mA. Both for TEM and XRD analysis the samples were loaded into airtight sample holders whilst in the glovebox. Thermo Gravimetric Analysis (TGA) of particle samples under air was performed using a PerkinElmer TGA7 thermo gravimetric analyzer. By increasing the temperature under air, all the silicon is eventually oxidised. Some samples were dissolved in 1 M KOH. After dilution up to 100 mL, the concentration of Si in the resulting solution was determined using Inductively Coupled Plasma-Optical Emission Spectroscopy (ICP-OES) on a PerkinElmer Optima 3000dv.

Results and discussion

Production rate

Initially the intrinsic (pure, i.e., not doped) silicon rods were used as electrodes. Typical voltage and current waveforms are given in Fig. 2 for a capacitance of 20 nF and 2 mm gap spacing. For comparison, typical data for the magnesium rods is given as well. For the magnesium electrodes both the current and voltage oscillate, the discharge ceases after
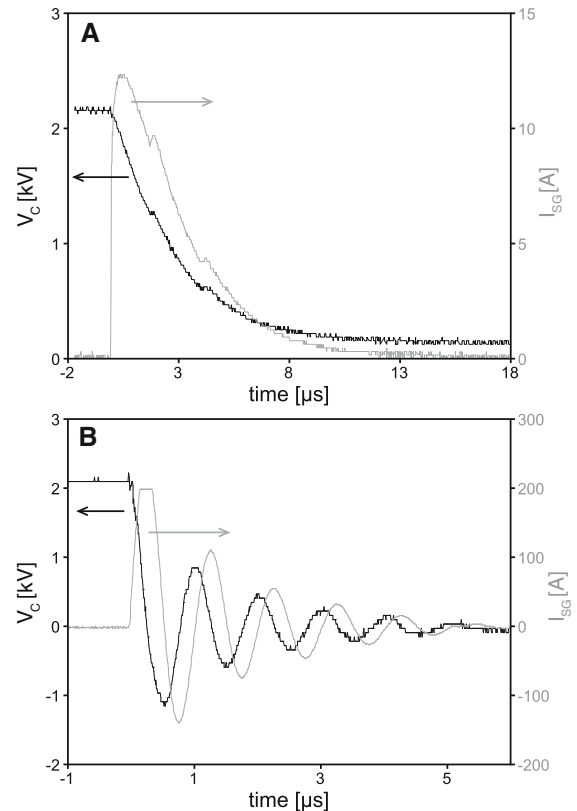

Fig. 2 **a** Capacitor voltage V_C and discharge current I_{SG} for intrinsic silicon electrodes in argon for 20 nF capacitance, 2 mm gap spacing. **b** V_C and I_{SG} for magnesium electrodes under the same conditions. In the case of the magnesium spark, the current exceeded 200 A, and with a probe giving an output of 0.1 V per ampere, the probe voltage exceeded 20 V, which is the maximum of the oscilloscope used. This results in clipping of the current peak during the first half-cycle

∼5 μs, and the current through the discharge reaches values of over 200 A. During several studies, we have consistently seen similar behaviour for many other metals including Cu, Pd, and Pt. In the case of the intrinsic silicon electrodes, however, there is no oscillation. Instead, a gradual decrease of the voltage is seen. The discharge lasts 12–14 μs, and most notably the discharge current is only ∼12 A.

Previous work (Tabrizi et al. 2009a) has shown that the oscillating behaviour of voltage and current during a metal electrode spark discharge can adequately be modelled by using a simple equivalent circuit for the capacitor, spark gap, and associated circuitry (Fig. 3). During the discharge, the spark gap behaves purely resistively with a value R_{SG}, i.e., the plasma has no significant inductive component.
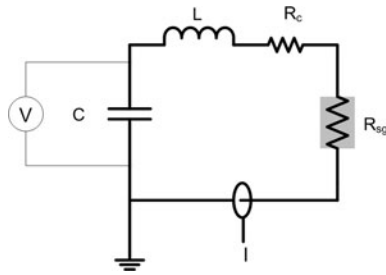
Fig. 3 Equivalent circuit for the spark generator during discharge. The location of the voltage (V) and current (I) measurement probes is indicated. C is the total capacitance of the capacitor bank and the associated circuitry, but is assumed to be equal to the capacitor bank capacitance, L is the inductance of the lines from the capacitor bank to the spark generator, R_C is the resistance of the circuit, and R_{SG} is the resistance of the spark gap

A second-order differential equation is then obtained for the charge Q on the capacitor,

$$L\frac{\mathrm{d}^2Q}{\mathrm{d}t^2} + R\frac{\mathrm{d}Q}{\mathrm{d}t} + \frac{Q}{C} = 0 \qquad (1)$$

where R is the sum of the spark resistance and the circuit resistance, L the inductance of the cable used and C the capacitance. Time is set $t = 0$ when breakdown occurs. At this point, the capacitor bank is charged to V_0, the discharge voltage, and there is as yet no current flowing. Then, depending on the values of R, L, and C, several solutions can be distinguished:

1. $R^2 - 4L/C < 0$ underdamped system
2. $R^2 - 4L/C = 0$ critically damped system
3. $R^2 - 4L/C > 0$ overdamped system

For metals the total resistance, determined from the electrical response, is of the order 1–5 Ω. Since there was practically no circuit resistance (R_c), this is purely the resistance of the plasma in the spark gap (R_{SG}). Due to the low resistance, an underdamped, oscillating system is obtained.

Apart from the silicon electrodes themselves, the power supply, capacitor bank and associated circuitry used for the silicon discharge were exactly the same as in the case of the metal electrodes, so the same equivalent circuit should be applicable apart from the Si electrode resistance. As no oscillatory behaviour is observed, we conclude that the high resistance of intrinsic silicon electrodes leads to overdamped behaviour. A fit of the overdamped solutions of Eq. 1 to the measured voltage and current waveforms
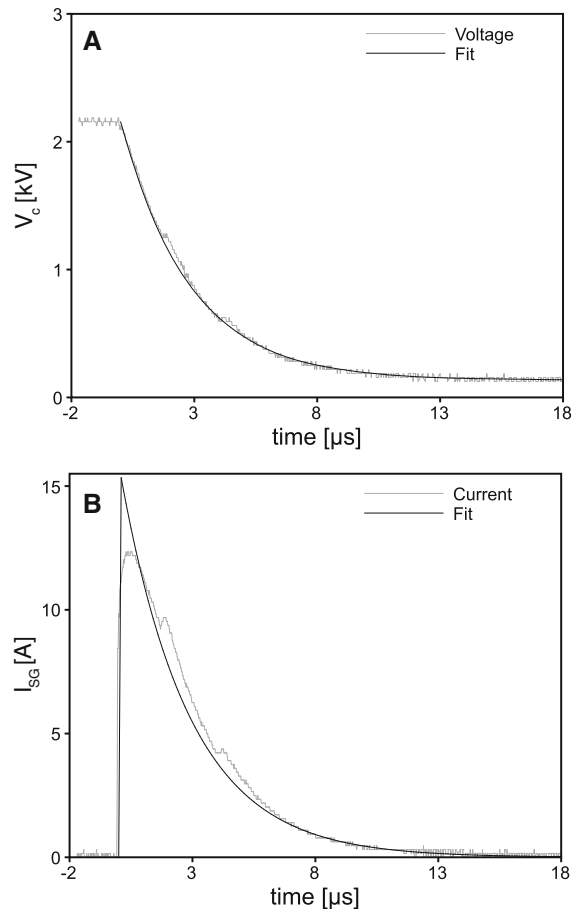

Fig. 4 **a** Fit of capacitor voltage V_C using the underdamped model. **b** Fit of the discharge current I_{SG}. Si electrodes, 2 mm gap spacing, 1.6 SLM Ar 5.0

for intrinsic silicon is given in Fig. 4. The fit is reasonable, and some deviation of the model from the experiment seen at the start of the discharge is explainable by the finite time the resistance requires to go from infinity (non-conducting) to finite values by heating of the gas between the electrodes. The best fit is obtained for a resistance of 130 Ω for the electrodes and the plasma combined. Previous results on magnesium sparks suggest a constant electron density and resistivity in spark plasmas. Based on these results we estimate the resistance of the plasma to be $\sim$20 Ω. This leaves $\sim$110 Ω for the resistance of the intrinsic silicon rods.

As the resistivity of intrinsic silicon is 2.3×10^5 Ω cm at 300 K (Zhang 2001), the total resistance of these rods should be $\sim$4 MΩ. Clearly, the model indicates an extreme reduction of the resistance due to

heating. The resistance of silicon drops rapidly with increasing temperature, due to an increase in electron and hole concentration. The electrodes heat due to the electric current. The value of $\sim 110\ \Omega$ from fitting experiment to model implies a temperature of $\sim 300\ °C$, which appears reasonable. UV light generated by the spark plasma may also play a role. It is absorbed in the surface layer of the electrodes, where it raises electrons from the valence to the conduction band, adding to the total charge carrier concentration, and lowering the resistivity.

In the case of metal electrodes, all the energy stored in the capacitors goes into the spark gap, where interaction of the plasma with the electrodes occurs through so-called hot spots. The high current densities reached in these hot spots result in ionic and Joule heating (Soldera et al. 2005), which in turn results in material evaporation. For silicon the resistance of the electrodes dissipates a large part of the energy. Photographs of both the silicon and magnesium sparks in Fig. 5 show the much lower intensity of the silicon spark. Furthermore, the high resistivity of the silicon causes the plasma to spread out over the surface of the electrode. This results in a lower current density. The energy that is put in the plasma is spread over more material, which can be cooled more effectively by conductive heat transfer to the bulk of the silicon. Since the duration of the discharge is also longer, the energy input *rate* is smaller as well, giving the material more time to conduct away the heat from the interaction area. All these effects combined result in lower temperatures being reached on the electrode surface and hence evaporation of less material. Indeed, measured particle size distributions (Fig. 6) clearly illustrate the very low mass production rate for Si particles. For comparison, a particle size distribution for magnesium is given as well. Both the maximum concentration and the median mobility particle size obtained for Mg electrodes are a factor 10 higher than for silicon, implying a mass production rate that is several orders of magnitude higher. Note that the particles are agglomerated, and the size distribution does not reflect the primary particle sizes.

The key to increasing the nanoparticle production rate from silicon or any other semiconductor lies in reducing the resistance of the electrodes. The circuit resistance induced by the semiconductor electrodes can in principle be reduced by heating to increase the intrinsic conductivity, changing the geometry of the
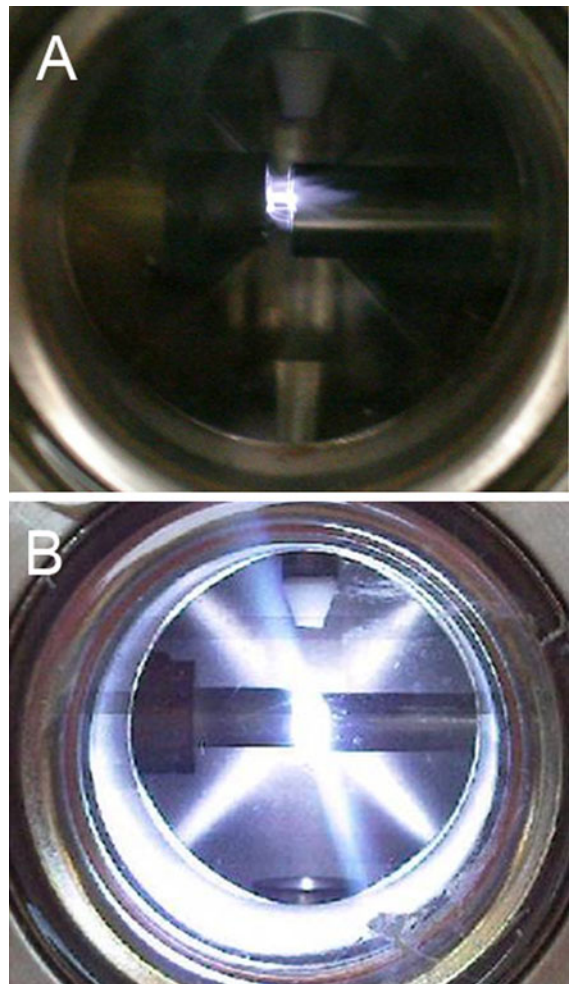

Fig. 5 a Photographs of an intrinsic silicon discharge. **b** photograph of a magnesium discharge. Note the difference in light intensity of the plasma; the light intensity of the spark between magnesium electrodes overloads the camera, the actual spark channel is much narrower

electrodes to reduce the path length of the current through the silicon, or by doping to introduce charge carriers. Some attempts were made to reduce the length of intrinsic silicon rods and hence decrease the resistance. Sparking between thin (1 mm) silicon wafers resulted in holes being formed in the wafers during the first few sparks. Subsequent sparks are localised to these holes, and these results in the formation of nanoparticles from the metal supports of the electrodes.

Heating of the intrinsic electrodes would have required a redesign of the experimental setup, while doped rods could be applied in our existing system.
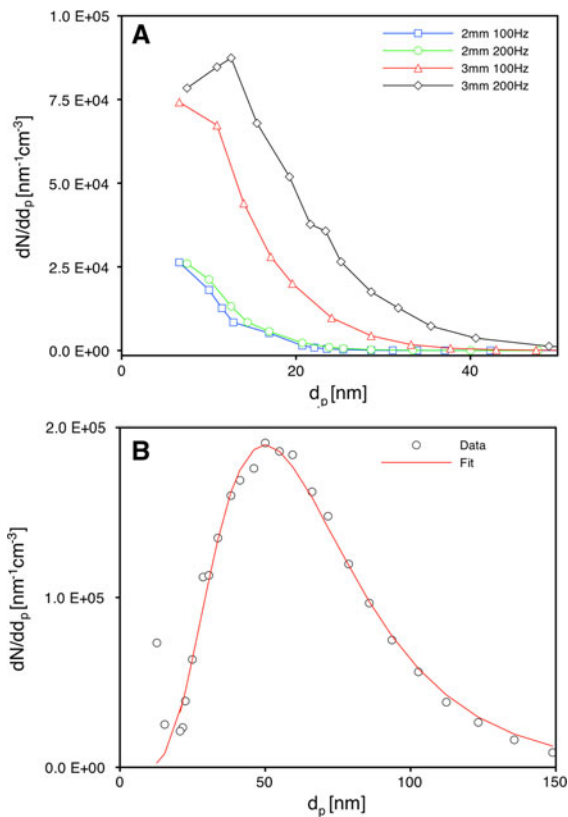
Fig. 6 **a** Particle size distributions for different gap spacings and discharge frequencies for silicon electrodes in Ar at 1.6 SLM. Large parts of the curves are smaller than the smallest size measurable with the TSI 3071 DMA. *Lines* between the measured data points merely serve as visual aids. **b** PSD for magnesium at 2 mm gap spacing and 200 Hz. The magnesium data is fitted by a log-normal curve (plotted in *red*). Note the large differences in both number concentration and equivalent mobility diameter of the particles between Si and Mg. Note that the particles are agglomerated as will be shown in the TEM micrographs of Fig. 9, and hence the size distribution does not reflect the primary particle sizes
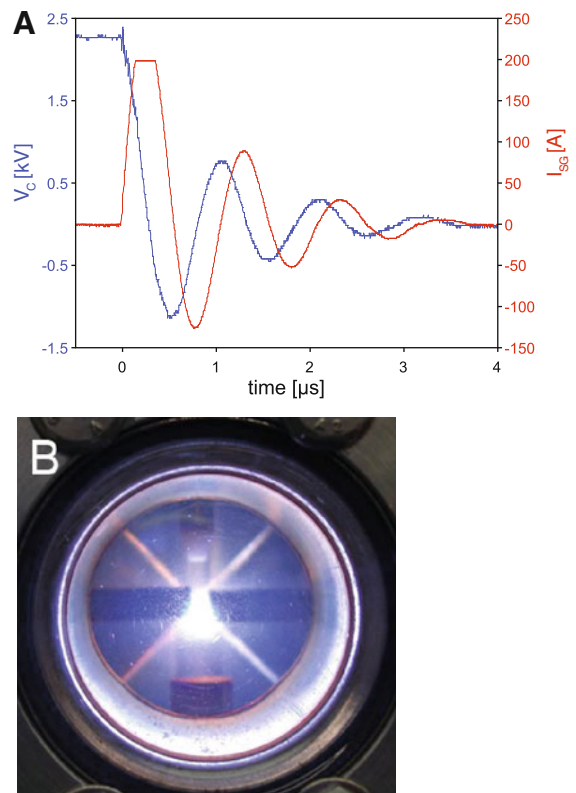

Fig. 7 **a** Discharge voltage and current for boron-doped Si rods in 1.6 SLM Ar 5.0, 2 mm gap spacing. **b** photograph of the spark discharge between doped rods

We used a set of 6 mm diameter boron (p)-doped electrodes with total length of 6 cm with a (measured) resistivity of 0.17 Ω cm. From the oscillating current and voltage of the discharge between these rods (Fig. 7), the effect of the reduced resistance of the doped material is visible. The discharge lasts ~ 4 μs and the current reaches values of over 200 A. A photograph of the spark discharge between doped rods also given in Fig. 7 shows that the spark is much more intense compared to intrinsic Si rods. From a fit of the voltage and current using the underdamped

RLC model (not shown), the resistance of the spark and the rods together was 2.4 Ω. The effect on the particle size distribution is dramatic, as can been seen in Fig. 8. This figure shows the size distributions of strongly agglomerated particles. It can be conferred that the mass production rate has increased by at least a factor of 10^3 and appears comparable to that of magnesium under similar conditions.

The boron dopant will also end up in the final product. The room temperature resistivity of these rods, ~ 0.17 Ω cm, corresponds to a dopant concentration of $\sim 10^{15}$ boron atoms cm^{-3} according to the curves given by Thurber et al. (1980). Given a concentration of 5×10^{22} Si atoms cm^{-3} for silicon (Zhang 2001) this means that the boron concentration is ~ 2 ppm. Hence the material is ~ 99.9999 wt% pure, and likely contains less than a single boron atom per particle. In comparison, most metals used as electrodes in the spark generator have a purity of $\sim 99.9\%$.
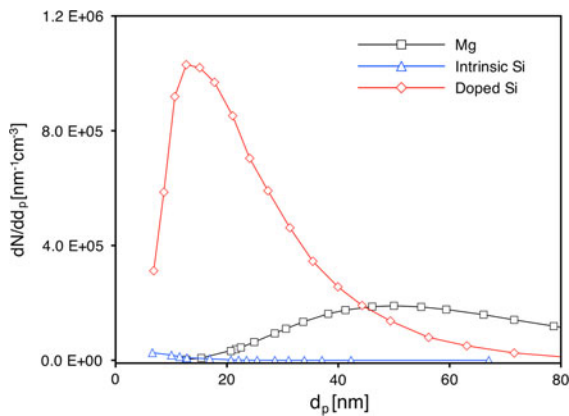
Fig. 8 Particle size distribution for intrinsic and doped Si electrodes in Ar 5.0, 2 mm gap spacing, $I_c = 5$ mA. For comparison the log-normal fit for magnesium under comparable settings, which was already shown in Fig. 4 is included as well. Note that the particles are agglomerated, and the size distribution does not reflect the primary particle sizes

Production of silicon nanoparticles

Using the boron-doped rods, particles were collected and analysed as described in the experimental section. TEM analysis reveals the typical fractal-like structure of agglomerates that form by diffusion-limited aggregation (Fig. 9). The visible lattice lines confirm the presence of crystalline material; the spacing distance is 3.18 Å, close to the theoretical value of 3.13 Å between the (111) Si crystalline planes (Zhang 2001). Since only a limited amount of crystal lattices were observed no conclusions can be drawn regarding the total fraction of crystalline material from the HRTEM micrographs alone. The primary particle diameters are quite uniform, as typical for spark-generated particles. The size is between 3 and 5 nm both for a gap distance of 2 and 3 mm. Hence the gap spacing does not appear to have a significant influence on the primary particle size, only on the production rate.

In addition, larger primary particles of 50–200 nm are observed in very low number. Due to Joule heating and ionic impact the hot spots (see above) of several square microns cross section (Soldera et al. 2004, 2005; Cundall and Craggs 1955) on the electrode surface are heated to high temperatures very quickly, causing the material to melt and partly evaporate. When the plasma dies out, the pressure that it exerted on the liquid metal pools is removed.

If the recoil force of the molten liquid pool is occasionally sufficient to overcome the surface tension of the liquid, this causes droplets of liquid material to be expelled from the electrode (Gray and Pharney 1974; Soldera et al. 2004, 2005). Evidently, the liquid usually resolidifies when the plasma dies out. Any ejected liquid droplets, cool off and solidify, resulting in round micron-sized particles. Tabrizi et al. (2009) already reported the formation of large metal particles by liquid metal pool formation and ejection from the electrodes. The large particles appear to occur more frequently at 3 mm instead of 2 mm gap spacing, likely due to the increased energy input. A larger gap requires a larger discharge voltage resulting in more energy being released from the capacitor.

XRD analysis was performed on the powder deposited on a membrane filter. The spectrum of the blank filter was subtracted from the XRD spectrum, which then shows peaks corresponding to the (111), (220) and (311) crystallographic planes of Si (Fig. 10). The XRD diffractogram hence suggests some crystallinity. The limited amount of material does however not allow solid conclusions about the total crystalline content. Measurement of the photo-luminescence properties did reveal an absorption peak at 230 nm, resulting in light emission in the near-UV peaking at ~ 340 nm. Since the nanoparticles are not passivated the origin of the photoluminescence is most likely defect centres at the surface of the particles. More research is required to characterise the photoluminescence properties in detail.

As the particle composition basically equals the electrode composition, extreme purity can, in principle, be achieved. However, surface oxidation limits the purity of the product, and this may be undesired. Gas purity is a critical point and requires great care (see above). A simple indicator of surface oxidation is therefore of great value. Our experiments showed that the colour of the collected Si nanopowders is extremely sensitive to surface oxidation. Powders collected on the membrane filters had a very distinct appearance in different experimental runs. Differently coloured deposits were obtained, as can be seen for six consecutive samples in Fig. 11. Samples 1 and 5 show a very dark reddish-brown colour, samples 2, 3 and 4 appear more orange/red. Since sample 6, which is very light yellow, had been intentionally but slowly exposed to oxygen after the XRD spectrum of
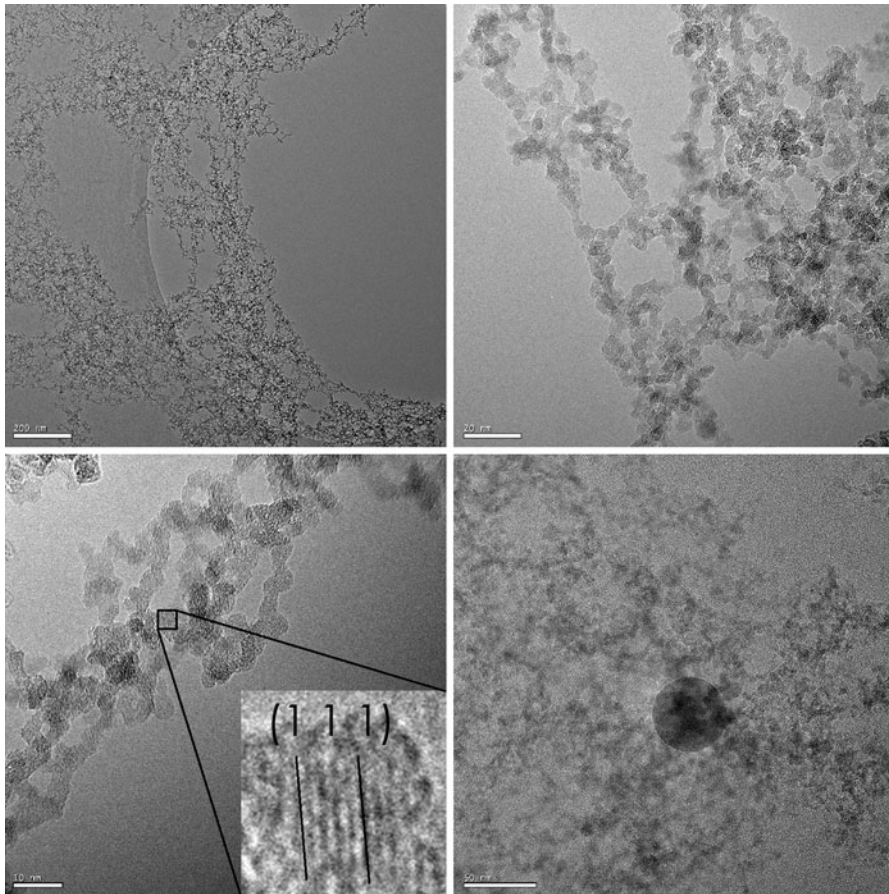
Fig. 9 TEM micrographs of nanoparticles produced from boron-doped silicon electrodes. Scale bars indicate (*clockwise from top left*) 200, 20, 50, and 10 nm. In the *bottom-right*

micrograph, an example of a larger spherical particle is given. The *inset* in the *bottom-left micrograph* shows the (111) Si crystal planes

Fig. 10 had been recorded, this suggests a relation between the colour of the powder and the degree of oxidation.

The following observations lead to a qualitative relation between colour and degree of oxidation. As soon as sample 1 was exposed to air, it visibly burned, i.e., the sample was pyrophoric. Sample 3 did not display any pyrophoric behaviour. We explain this by a protective oxide layer in this case, which guarantees that further oxidation proceeds slowly. In sample 1 such a layer is absent, which enables rapid oxidation the moment it is exposed to air. This exothermal reaction heats the sample, further accelerating the reaction, and good conditions for self-sustained burning are present. Thus, the dark brown colour of sample 1 indicates pure silicon, the red colour of sample 3 indicates an oxide layer and the

yellow colour of sample 6 indicates further oxidation. As a pure SiO_2 nanopowder looks white, the yellow colour is probably an indication of remaining Si cores, which are so well protected by the oxide that they virtually do not oxidise further.

Two samples were analysed using ICP-OES. First the initial mass m_0 of the samples was determined in the glovebox immediately after production. The particles are then taken out of the glovebox and dissolved in KOH. Both Si and any Si–O compounds dissolve well in KOH. The ICP-OES analysis yields the concentration of Si atoms in the solution, and, since the volume of the solution is accurately known, the mass of Si atoms in the sample (m_{Si}). The proportion of SiO_2 and Si can then be calculated under the assumption that only these two constituents were present in the original sample mass determined
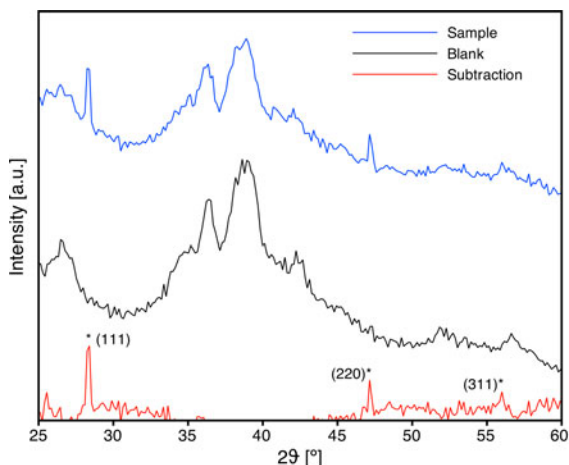
Fig. 10 XRD pattern of nanoparticles generated using boron-doped silicon electrodes. After subtraction of the filter background the characteristic Si peaks can be identified (see text)

Table 1 Results of ICP-OES analysis

Sample	m_0 (mg)	c_{Si} (mg/L)	wt% Si
4	1.4 ± 0.1	1.22	65–88
5	1.1 ± 0.1	1.17	95–100

in the glovebox. It must be emphasised that the oxidation taking place after the sample was removed from the glovebox (by contact with air, water and KOH) does not affect the outcome of the calculation; calculations are only based on m_0 (determined before oxidation) and m_{Si}. As SiO compounds are not volatile, oxidation will not change the total mass of silicon in the sample, only the oxygen content, and great care is taken to transfer the entire samples without loss into the KOH. Table 1 gives the result for samples 4 and 5. The uncertainty in the wt% corresponds to the accuracy of the balance used.

The analysis confirms that the oxide content of the darker coloured sample 5 is lower than that of sample 4. It indicates that the particles of sample 5 have less than a tenth of a monolayer of oxidised Si on their surface. This is in agreement with the pyrophoric nature of the dark brown sample 1. We conclude that the colour of a nanoparticulate Si powder is an

indicator of their degree of oxidation. Our observations are in line with studies on partly oxidised SiNPs prepared via laser vapourisation-controlled condensation (Li et al. 1999) and also with the oxidation of SiNPs having organic monolayers grafted to their surfaces (Hua et al. 2006). Remarkably, using a hot wire thermal catalytic pyrolysis process, darker colour powders (particle size ∼10 nm, 40% oxygen) were reported to contain more oxygen as compared to light-coloured Si powders (particle size ∼50 nm, 26% oxygen) (Scriba et al. 2008). This seems to be in contrast with our results, which show that the colour SiNPs changes from dark (grey/brown), via yellow, to white upon oxidation. The apparent discrepancy can be rationalised by the fact that the colour observed in nanoparticulate powders depends on particle size as well as on particle and powder composition and morphology in a complex way. For example, the electrical connectivity between the semiconductor cores should have an influence.

The differences in the degree of oxidation of the samples in Fig. 11 can qualitatively be explained as follows. Sample 1 had been collected after the setup had been running for several hours. This leads to pure particles, because the nanoparticulate agglomerates produced are extremely high surface area getters that scavenge any oxygen or water desorbing from the walls, thus cleaning the system. After this sample was collected, the spark generator had to be opened to remove particles built up around the electrodes. This causes undesired arcing between the high voltage
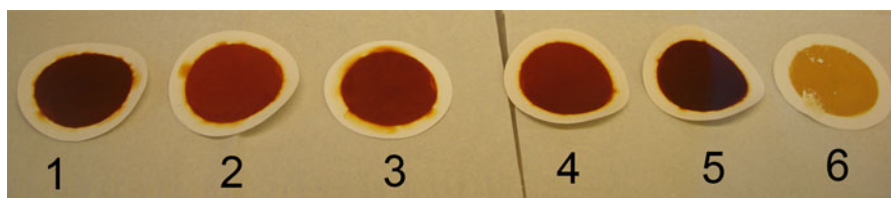

Fig. 11 Colour of the particles as deposited on membrane filters; photograph taken through the window of the glovebox. *Samples 1–5* had been stored in the glovebox, and still have the same colour in the photograph as they had immediately after

production. *Sample 6*, which is very *light yellow*, had been slowly exposed to air after the XRD analysis. See text for further sample specifications. Please refer to the electronic version of the article for the colour representation

electrode and the housing. During opening, exposure of the inner surfaces of the spark generator to oxygen and especially water occurs. Although the system underwent a vacuum bake at 100 °C, this was apparently not sufficient to remove of all the impurities, since sample 2, 3 and 4 are clearly more oxidised than sample 1. The continuing gettering action of the nanoparticles eventually led to the purity of sample 5, where virtually all oxygen has been removed. As stated above, the discolouration of sample 6 was due to a slow, post-preparation oxygen exposure.

Whether or not spark discharge generation is suitable for the production of silicon particles depends on a particular application. In the case of battery- and hydrogen storage applications, the high elemental Si content of 95–100% implies more active material, which positively influences the energy content of both batteries and hydrogen storage materials. Since oxides inevitably act as diffusion barriers, their reduction or total elimination also result in higher reaction rates. With careful working and relatively simple measures, for instance longer bake-out processes at even lower pressures and replacement of all the permeable O-rings in the setup, the purity can likely be further increased.

Liquid phase methods (O'Farrell et al. 2006) involve the use of silicon tetrachloride or organosilane compounds, the use of which can result in the inclusion of impurities in the particles and leads to bigger waste streams. These impurities will also reduce the available active material and hence the energy content. Spark Discharge generation offers the elimination of chemicals and solvents. Compared to liquid phase methods the production rate is, however, currently very low, the laboratory scale production rate is only of the order of 1 mg h^{-1}. Significant increases in the production rate are thus needed, since battery- or hydrogen storage related applications require rather sizeable quantities of materials. For this reason, much of the work currently undertaken in our laboratory is focused on upscaling the production rate of spark discharge generation. This by increasing the energy input per spark, the number of sparks per second and the number of spark gaps.

Furthermore and perhaps more importantly, both batteries and metalhydride based hydrogen storage systems consist of a mix of materials. The mixing of the materials directly affects the performance, since

diffusion of metal atoms is required (lithium in the case of batteries, and magnesium in the case of Mg–Si-based hydrogen storage materials). By using two different electrodes, for instance, one magnesium and one silicon electrode in a single spark gap, the materials are mixed on a near-atomic scale in the plasma plumes emanating from the electrodes. This severely reduces metal diffusion paths and further increases reaction rates. Both for liquid-based methods and a method like electrochemical etching followed by sonification it is much harder to sufficiently mix the nanoparticle on this very small scale.

For sensor applications, the low production rate is not a problem, as even the currently still limited laboratory scale production rate can provide sufficient material for sensor production. The possibility of continuous operation, direct functionalisation and application of the particles through impaction, makes spark discharge especially suited for sensor applications. The ability to directly focus and manipulate a particle beam allows for very controlled deposition of the nanoparticles on the sensor surface. This results in dependable sensor operation and at the same time very limited material use, while the very small particle size leads to rapid sensor response. Liquid-based methods and electrochemical etching cannot be integrated with impaction, but it is true that other aerosol-based methods like laser ablation or laser pyrolysis can. The choice for spark discharge versus one of these methods then depends on the achievable particle size, familiarity with the production process but not in the least also the complexity of the various setups. We feel that the simplicity of the spark discharge setup is a distinct advantage, as there is for instance less need for safety measures related to the use of silane and lasers with spark discharge.

Conclusions

The mass production rate of silicon nanoparticles from intrinsic silicon electrodes by spark discharge is orders of magnitude smaller compared to metals, since less energy goes into a larger area at a slower rate. Analysis using a simple equivalent circuit model indicates that this is due to the higher resistance of a semiconductor with respect to a metal. Replacing intrinsic silicon by boron-doped rods results in a 1000-fold increase in mass production. Particles can

thus be generated from any semiconductor using spark discharge, as long as the resistance is kept sufficiently low by either n- or p-doping, heating the electrodes, or changing their shape to reduce the current path-length. Transmission electron micrographs revealed a rather narrow size distribution, comparable to those SPG-prepared metal particles. Based on earlier work on metal particles (Tabrizi et al. 2009a), we expect that also in the case of semiconductors the mean particle size can be controlled by tuning the energy per spark.

By taking stringent measures to reduce the ingress of oxygen and water into the setup, the production of virtually pure, unoxidised silicon particles with a primary particle size of 3–5 nm is possible using the doped Si rods. Here the gettering action of the particles themselves can be used. We have observed a clear correlation between the colour of the particles and the degree of oxidation. Through basic understanding or through calibration, together with an appropriate spectrometer, this effect could be used for quantitative determination of degree of oxidation.

In conclusion, spark discharge nanoparticle generation is introduced as a new technique for the production of extremely small, uniformly sized and very pure silicon nanoparticles. This continuous technique can be combined with other steps, e.g. surface functionalization (Li 2004) or the immediate impaction of freshly prepared nanoparticles onto a substrate for applications. The small size of the spark discharge produced nanoparticles allows for rapid reaction rates in for instance battery, hydrogen storage or sensor applications.

References

Arico AS, Bruce P, Scrosati B, Tarascon J-M, van Schalkwijk W (2005) Nanostructured materials for advanced energy conversion and storage devices. Nat Mater 4(5):366–377. doi:10.1038/nmat1368

Asefa T, Duncan CT, Sharma KK (2009) Recent advances in nanostructured chemosensors and biosensors. Analyst 134(10):1980–1990. doi:10.1039/B911965P

Aswal DK, Lenfant S, Guerin D, Yakhmi JV, Vuillaume D (2006) Self assembled monolayers on silicon for molecular electronics. Anal Chim Acta 568(1–2):84–108. doi:10.1016/j.aca.2005.10.027

Ben-Chorin M, Kux A, Schechter I (1994) Adsorbate effects on photoluminescence and electrical conductivity of porous silicon. Appl Phys Lett 64(4):481–483. doi:10.1063/1.111136

Biskos G, Kovacik P, Schmidt-Ott A (2010) A new particle based gas sensor concept applied to hydrogen. Paper presented at the world conference on particle technology, Neuremburg, Germany, April 26–29

Burda C, Chen X, Narayanan R, El-Sayed MA (2005) Chemistry and properties of nanocrystals of different shapes. Chem Rev 105(4):1025–1102. doi:10.1021/cr030063a

Buriak JM (2002) Organometallic chemistry on silicon and germanium surfaces. Chem Rev 102(5):1271–1308. doi:10.1021/cr000064s

Burns A, Ow H, Wiesner U (2006) Fluorescent core-shell silica nanoparticles: towards "lab on a particle" architectures for nanobiotechnology. Chemical Society Reviews 35(11):1028–1042

Byeon JH, Park JH, Hwang J (2008) Spark generation of monometallic and bimetallic aerosol nanoparticles. J Aerosol Sci 39(10):888–896. doi:10.1016/j.jaerosci.2008.05.006

Canham LT (1990) Silicon quantum wire array fabrication by electrochemical and chemical dissolution of wafers. Appl Phys Lett 57(10):1046–1048. doi:10.1063/1.103561

Cundall CM, Craggs JD (1955) Electrode vapour jets in spark discharges. Spectrochim Acta 7(3):149–152. doi:10.1016/0371-1951(55)80018-5

De M, Ghosh PS, Rotello VM (2008) Applications of nanoparticles in biology. Adv Mater 20(22):4225–4241. doi:10.1002/adma.200703183

Ding N, Xu J, Yao Y, Wegner G, Lieberwirth I, Chen C (2009) Improvement of cyclability of si as anode for li-ion batteries. J Power Sources 192(2):644–651. doi:10.1016/j.jpowsour.2009.03.017

Foucaran A, Pascal-Delannoy F, Giani A, Sackda A, Combette P, Boyer A (1997) Porous silicon layers used for gas sensor applications. Thin Solid Films 297(1–2):317–320. doi:10.1016/s0040-6090(96)09437-0

Ghoshal S, Mitra D, Roy S, Dutta Majumder D (2010) Biosensors and biochips for nanomedical applications: a review. Sens Tranducers J 113(2):1–17

Goesmann H, Feldmann C (2010) Nanoparticulate functional materials. Angew Chem Int Ed 49(8):1362–1395. doi:10.1002/anie.200903053

Gray EW, Pharney JR (1974) Electrode erosion by particle ejection in low-current arcs. J Appl Phys 45(2):667–671. doi:10.1063/1.1663300

Günes S, Neugebauer H, Sariciftci NS (2007) Conjugated polymer-based organic solar cells. Chem Rev 107(4):1324–1338. doi:10.1021/cr050149z

Hua F, Erogbogbo F, Swihart MT, Ruckenstein E (2006) Organically capped silicon nanoparticles with blue photoluminescence prepared by hydrosilylation followed by oxidation. Langmuir 22(9):4363–4370. doi:10.1021/la0529106

Janot R, Cuevas F, Latroche M, Percheron-Guégan A (2006) Influence of crystallinity on the structural and hydrogenation properties of Mg_2x phases (x = Ni, Si, Ge, Sn). Intermetallics 14(2):163–169. doi:10.1016/j.intermet.2005.05.003

Kasavajjula U, Wang C, Appleby AJ (2007) Nano- and bulk-silicon-based insertion anodes for lithium-ion secondary cells. J Power Sources 163(2):1003–1039. doi:10.1016/j.jpowsour.2006.09.084

Létant S, Sailor MJ (2000) Detection of hf gas with a porous silicon interferometer. Advanced Materials 12(5): 355–359. doi:10.1002/(SICI)1521-4095(200003)12:5<355::AID-ADMA355>3.0.CO;2-H

Li S, Germanenko IN, El-Shall MS (1999) Nanoparticles from the vapor phase: Synthesis and characterization of si, ge, MoO_3, and WoO_3 nanocrystals. J Clust Sci 10(4): 533–547. doi:10.1023/a:1021957108775

Li X, He Y, Swihart MT (2004) Surface functionalization of silicon nanoparticles produced by laser-driven pyrolysis of silane followed by HF-HNO3 etching. Langmuir 20:4720–4727. doi:10.1021/la036219j

Liao Y-C, Roberts JT (2006) Self-assembly of organic monolayers on aerosolized silicon nanoparticles. J Am Chem Soc 128(28):9061–9065. doi:10.1021/ja0611238

Masala O, Seshadri R (2004) Synthesis routes for large volumes of nanoparticles. Annual Review of Materials Research 34(1):41–81. doi:10.1146/annurev.matsci.34.052803.090949

Nayfeh OM, Rao S, Smith A, Therrien J, Nayfeh MH (2004) Thin film silicon nanoparticle UV photodetector. Photonics Technology Letters. IEEE 16(8):1927–1929 10.1109/LPT.2004.831271

O'Farrell N, Houlton A, Horrocks BR (2006) Silicon nanoparticles: applications in cell biology and medicine. International journal of Nanomedicine 1(4):451–472. doi:10.2147/IJN.S

Peineke C, Schmidt-Ott (2006) A highly porous nanostructured materials from impacted nanoparticles. In Biswas P, Chen D-R, Hering S (eds) Proceedings of 7th international aerosol conference. American Association for Aerosol Research

Schwyn S, Garwin E, Schmidt-Ott A (1988) Aerosol generation by spark discharge. J Aerosol Sci 19(5):639–642. doi:10.1016/0021-8502(88)90215-7

Scriba MR, Arendse C, Härting M, Britton DT (2008) Hot-wire synthesis of si nanoparticles. Thin Solid Films 516(5):844–846. doi:10.1016/j.tsf.2007.06.191

Simonin L, Lafont U, Tabrizi N, Schmidt-Ott A, Kelder EM (2007) Sb/o nano-composites produced via spark discharge generation for li-ion battery anodes. J Power Sources 174(2):805–809. doi:10.1016/j.jpowsour.2007.06.197

Soldera FA, Mucklich FT, Hrastnik K, Kaiser T (2004) Description of the discharge process in spark plugs and its correlation with the electrode erosion patterns. IEEE Trans Veh Technol 53(4):1257–1265. doi:10.1109/TVT.2004.830977

Soldera F, Lasagni A, Mucklich F, Kaiser T, Hrastnik K (2005) Determination of the cathode erosion and temperature for the phases of high voltage discharges using fem simulations. Comput Mater Sci 32(1):123–139. doi:10.1016/j.commatsci.2004.06.004

Tabrizi NS (2009) Generation of nanoparticles by spark discharge. Delft University of Technology, Delft

Tabrizi NS, Ullmann M, Vons VA, Lafont U, Schmidt-Ott A (2009a) Generation of nanoparticles by spark discharge. J Nanopart Res 11(2):315–332. doi:10.1007/s11051-008-9407-y

Tabrizi NS, Xu Q, van der Pers NM, Lafont U, Schmidt-Ott A (2009b) Synthesis of mixed metallic nanoparticles by spark discharge. J Nanopart Res 11(5):1209–1218. doi:10.1007/s11051-008-9568-8

Tabrizi NS, Xu Q, van der Pers N, Schmidt-Ott A (2010) Generation of mixed metallic nanoparticles from immiscible metals by spark discharge. J Nanopart Res 12(1): 247–259. doi:10.1007/s11051-009-9603-4

Thurber WR, Mattis RL, Liu YM, Filliben JJ (1980) Resistivity-dopant density relationship for boron-doped silicon. J Electrochem Soc 127(10):2291–2294. doi:10.1149/1.2129394

Watanabe K, Okada T, Choe I, Sato Y (1996) Organic vapor sensitivity in a porous silicon device. Sens Actuators B 33(1–3):194–197. doi:10.1016/0925-4005(96)80097-9

Wiedensohler A, Fissan HJ (1988) Aerosol charging in high purity gases. J Aerosol Sci 19(7):867–870. doi:10.1016/0021-8502(88)90054-7

Wiedensohler A, Fissan HJ (1991) Bipolar charge distributions of aerosol particles in high-purity argon and nitrogen. Aerosol Sci Technol 14(3):358–364. doi:10.1080/02786829108959498

Zhang XG (2001) Electrochemistry of silicon and its oxide. Kluwer Academic/Plenum, New York